Exciton-photon, exciton-phonon matrix elements, and resonant Raman intensity of single-wall carbon nanotubes

J. Jiang,[1] R. Saito,[1] K. Sato,[1] J. S. Park,[1] Ge. G. Samsonidze,[2] A. Jorio,[3] G. Dresselhaus,[4] and M. S. Dresselhaus[2,5]

[1]*Department of Physics, Tohoku University and CREST JST, Sendai 980-8578, Japan*

[2]*Department of Electrical Engineering and Computer Science, Massachusetts Institute of Technology, Cambridge, Massachusetts 02139-4307, USA*

[3]*Departamento de Física, Universidade Federal de Minas Gerais, Belo Horizonte, MG, 30123-970, Brazil*

[4]*Francis Bitter Magnet Laboratory, Massachusetts Institute of Technology, Cambridge, Massachusetts 02139-4307, USA*

[5]*Department of Physics, Massachusetts Institute of Technology, Cambridge, Massachusetts 02139-4307, USA*

Within the framework of the tight-binding model, we have developed exciton-photon and exciton-phonon matrix elements for single-wall carbon nanotubes. The formulas for first-order resonance and double-resonance Raman processes are discussed in detail. The lowest-energy excitonic state possesses an especially large exciton-photon matrix element compared to other excitonic states and continuum band states because of its localized wave function with no node. Unlike the free-particle picture, the photon matrix element in the exciton picture shows an inverse diameter dependence but no tube type or chirality dependences. As a result, the optical absorption intensity shows a strong diameter dependence but no tube type or chirality dependences. Moreover, the continuum band edge can be determined from the wave function or exciton-photon matrix element. For the radial breathing mode (RBM) and G-band modes, the phonon matrix elements in the exciton and free-particle pictures are almost the same. As a result, the intensity for the Kataura plots for the RBM or G-band modes by the exciton and free-particle pictures show similar family patterns. However, the excitonic effect has greatly increased the diameter dependence and magnitude of the intensities for the RBM and G band by enhancing the diameter dependence and magnitude of the photon matrix element. Therefore, excitons have to be considered in order to explain the strong diameter dependence of the Raman signal observed experimentally.

I. INTRODUCTION

Single-wall carbon nanotubes (SWNTs) can be characterized by two integers (n,m) that define both their diameter and chirality, and $2n+m=3p+r$, where p is an integer and $r=0,1,2$ defines whether they are metallic (M) or semiconducting type I (SI) or type II (SII) SWNTs, respectively.[1–4] The optical spectroscopies of SWNTs have received increasing attention for assigning the chirality (n,m) of the SWNTs and studying the physics of these one-dimensional (1D) systems.[2,3,5–10]

Recent theories and experiments on carbon nanotubes support a picture where excitonic effects are important to optical spectroscopy. Strongly bound excitons are predicted for small-diameter S-SWNTs and these predictions are confirmed by experiments.[11–18] An exciton plus a phonon sideband, which is peaked at around 200 meV above the main absorption peak, was found in the absorption spectra of SWNTs, and was explained by strong effects in the exciton-phonon coupling.[18,19]

So far, all Raman scattering theories that have been proposed are based on a free-particle picture. Since excitonic effects are important in the optical properties of SWNTs, it is interesting to study Raman scattering from an excitonic picture. Moreover, a very well pronounced qualitative effect has recently been observed in the Raman intensity from the radial breathing mode (RBM) of SWNTs.[2,20] The RBM intensity shows a well-defined dependence on tube type (SI or SII

tube), diameter, and chiral angle.[2] This qualitative phenomenon has been explained by Raman intensity calculations within the free-particle picture.[2,21,22] A detailed analysis indicates that the free-particle picture can generally describe the tube type and chiral angle dependences, although it underestimates the diameter dependence, especially for small-diameter SWNTs.[23] Thus, it should be interesting to understand from an excitonic picture the reasons for this underestimate of the diameter dependence.

We have developed computer programs to calculate the exciton energies and wave functions by solving the Bethe-Salpeter (BS) equation within the simple and extended tight-binding (STB and ETB) models.[24] A $2n+m=$constant family behavior is found in the exciton wave function localization length, binding energy, and environment-induced energy shift.[24] A Kataura plot within the exciton picture is also given.[24] Our calculated results agree well with the two-photon experimental results.[13,14,25] Moreover, we have developed computer programs to calculate the electron-photon (el-op) and electron-phonon (el-ph) matrix elements.[21,26–33]

In this paper, we further develop the exciton-photon (ex-op) and exciton-phonon (ex-ph) matrix elements. We then apply these matrix elements to both resonance and double resonance Raman processes. The chirality dependence of the matrix elements in the exciton picture is then compared with those in the free-particle picture. The relationship between the Raman intensities by the exciton and free-particle pictures is then revealed.

As we have pointed out in our previous papers,[24,26,31] the STB model can well describe the exciton wave function and el-op matrix element and can approximately describe the el-ph matrix elements. In this paper, for simplicity, we will calculate the ex-op and ex-ph matrix elements in the framework of the STB model. The extension to the ETB model is straightforward and will be published elsewhere.

In Sec. II, we show how to calculate the ex-op and ex-ph matrix elements. In Sec. III, we calculate the matrix elements and resonance Raman intensities for the radial breathing mode and *G*-band (*A* symmetry) modes. The results in the exciton and free-particle pictures are compared. Finally, a summary is given.

II. THEORETICAL METHOD

A. Exciton-photon matrix element

We calculate the el-op matrix element $M_{\text{el-op}}$ in the dipole approximation[26,27,34]

$$M_{\text{el-op}} \propto \mathbf{D}(\mathbf{k}', \mathbf{k}) \cdot \mathbf{P}, \tag{1}$$

with $\mathbf{D}(\mathbf{k}', \mathbf{k}) = \langle \psi(\mathbf{k}') | \nabla | \psi(\mathbf{k}) \rangle$ being the dipole vector between the initial and final states, and $\mathbf{P}$ being the light polarization. In the case of parallel polarization, the selection rule for $\mathbf{k}$ gives $\mathbf{k}' = \mathbf{k}$, and we can write the el-op Hamiltonian as

$$H_{\text{el-op}} = \sum_{\mathbf{k}} D_{\mathbf{k}} c_{\mathbf{k}c}^{\dagger} c_{\mathbf{k}v} (a + a^{\dagger}), \tag{2}$$

where we have neglected a constant in the optical matrix element $M_{\text{el-op}}$, $D_{\mathbf{k}}$ is the *z* component of $\mathbf{D}(\mathbf{k}, \mathbf{k})$, $c_{\mathbf{k}c}^{\dagger}$ ($c_{\mathbf{k}v}$) is the electron creation (annihilation) operator in the conduction (valence) band, and $a^{\dagger}$ (a) is the photon creation (annihilation) operator.

The exciton wave function $|\Psi_{\mathbf{q}}^{n}\rangle$ with a center-of-mass momentum $\mathbf{q}$ can be expressed as

$$|\Psi_{\mathbf{q}}^{n}\rangle = \sum_{\mathbf{k}} Z_{\mathbf{k}c,(\mathbf{k}-\mathbf{q})v}^{n} c_{\mathbf{k}c}^{\dagger} c_{(\mathbf{k}-\mathbf{q})v} |0\rangle, \tag{3}$$

where $Z_{\mathbf{k}c,(\mathbf{k}-\mathbf{q})v}^{n}$ is the eigenvector of the *n*th ($n = 0, 1, 2, \dots$) state of the Bethe-Salpeter equation, and $|0\rangle$ is the ground state. The summation on $\mathbf{k}$ is taken for the two-dimensional Brillouin zone (2D BZ). However, in a previous paper, we have shown that the summation on a single cutting line of a *k* state is sufficient.[24] Due to momentum conservation, the photon-excited exciton is an exciton with $\mathbf{q} = 0$. From Eqs. (2) and (3), we get the ex-op matrix element between an excited state $|\Psi_{0}^{n}\rangle$ and the ground state $|0\rangle$,

$$M_{\text{ex-op}} = \langle \Psi_{0}^{n} | H_{\text{el-op}} | 0 \rangle = \sum_{\mathbf{k}} D_{\mathbf{k}} Z_{\mathbf{k}c,\mathbf{k}v}^{n*}. \tag{4}$$

As we know, a SWNT has A_1, A_2, E, and E^* symmetry excitons and only the A_2 exciton is bright, while the other A_1, E, and E^* excitons are dark.[24,35] Because of the two inequivalent *K* points in the 2D BZ of graphite, the A_1 and A_2 excitons are symmetric and antisymmetric under a C_2 rotation, respectively. The wave function for an A_1 (A_2) exciton with $\mathbf{q} = 0$ is given by
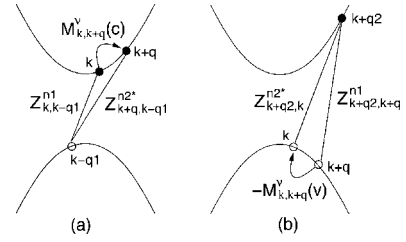
FIG. 1. (a) Electron and (b) hole scattering processes in the ex-ph matrix element for the first and second terms of Eq. (8). The matrix element for (a) and (b) is determined by the electron and hole matrix elements weighted by the wave function coefficients from the initial and final states.

$$|\Psi_{0}^{n}(A_{1,2})\rangle = \frac{1}{\sqrt{2}} \sum_{\mathbf{k}} Z_{\mathbf{k}c,\mathbf{k}v}^{n} (c_{\mathbf{k}c}^{\dagger} c_{\mathbf{k}v} \mp c_{-\mathbf{k}c}^{+} c_{-\mathbf{k}v}) |0\rangle, \tag{5}$$

where $\mathbf{k}$ and $-\mathbf{k}$ are around the *K* and *K'* points, respectively, and $-$ (+) in $\mp$ is for an A_1 (A_2) exciton.

When we use the relation $D_{\mathbf{k}} = D_{-\mathbf{k}}$, the ex-op matrix elements for the A_1 and A_2 excitons are given by

$$M_{\text{ex-op}}(A_1^n) = 0,$$

$$M_{\text{ex-op}}(A_2^n) = \sqrt{2} \sum_{\mathbf{k}} D_{\mathbf{k}} Z_{\mathbf{k}c,\mathbf{k}v}^{n*}. \tag{6}$$

Equation (6) directly indicates that A_1 excitons are dark and only A_2 excitons are bright, which is consistent with the predictions by group theory.[35]

B. Exciton-phonon matrix element

The Hamiltonian for the el-ph coupling for a phonon mode $(\mathbf{q}, \nu)$ has the form

$$H_{\text{el-ph}} = \sum_{\mathbf{k}\mathbf{q}\nu} [M_{\mathbf{k},\mathbf{k}+\mathbf{q}}^{\nu}(c) c_{(\mathbf{k}+\mathbf{q})c}^{\dagger} c_{\mathbf{k}c} - M_{\mathbf{k},\mathbf{k}+\mathbf{q}}^{\nu}(v) c_{(\mathbf{k}+\mathbf{q})v}^{\dagger} c_{\mathbf{k}v}]$$

$$\times (b_{\mathbf{q}\nu} + b_{\mathbf{q}\nu}^{\dagger}), \tag{7}$$

where $M(c)$ [$M(v)$] is the el-ph matrix element for the conduction [valence] band, and $b_{\mathbf{q}\nu}^{\dagger}$ ($b_{\mathbf{q}\nu}$) is a phonon creation (annihilation) operator for the νth phonon mode at $\mathbf{q}$.

From Eq. (7), we obtain the ex-ph matrix element between the initial state $|\Psi_{\mathbf{q}1}^{n1}\rangle$ and a final state $|\Psi_{\mathbf{q}2}^{n2}\rangle$,

$$M_{\text{ex-ph}} = \langle \Psi_{\mathbf{q}2}^{n2} | H_{\text{el-ph}} | \Psi_{\mathbf{q}1}^{n1} \rangle = \sum_{\mathbf{k}} [M_{\mathbf{k},\mathbf{k}+\mathbf{q}}^{\nu}(c) Z_{\mathbf{k}+\mathbf{q},\mathbf{k}-\mathbf{q}1}^{n2*} Z_{\mathbf{k},\mathbf{k}-\mathbf{q}1}^{n1}$$

$$- M_{\mathbf{k},\mathbf{k}+\mathbf{q}}^{\nu}(v) Z_{\mathbf{k}+\mathbf{q}2,\mathbf{k}}^{n2*} Z_{\mathbf{k}+\mathbf{q}2,\mathbf{k}+\mathbf{q}}^{n1}], \tag{8}$$

with $\mathbf{q} = \mathbf{q}2 - \mathbf{q}1$ giving the momentum conservation. The energy conservation for ex-ph scattering is given by $E_{\mathbf{q}2}^{n2} - E_{\mathbf{q}1}^{n1} = E_{\text{ph}}$ for phonon absorption, and $E_{\mathbf{q}1}^{n1} - E_{\mathbf{q}2}^{n2} = E_{\text{ph}}$ for phonon emission. In the following, we will consider only the Stokes (phonon emission) process and we will not explicitly write the phonon number in $|\Psi_{\mathbf{q}}^{n}\rangle$.

Figure 1 schematically illustrates the electron and hole scattering processes in the ex-ph matrix element, which corresponds to the first and second terms in Eq. (8), respec-
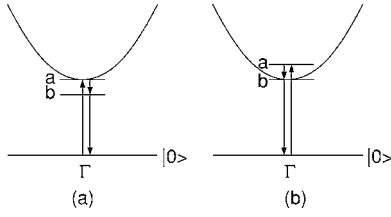
FIG. 2. First-order resonance Raman Stokes processes: (a) incident resonance process and (b) scattered resonance process.

tively. Figure 1(a) shows that the ex-ph matrix element from the electron scattering process is the el-ph matrix element $M^\nu_{\mathbf{k},\mathbf{k}+\mathbf{q}}(c)$ weighted by the wave function coefficient $Z^{n2*}_{\mathbf{k}+\mathbf{q},\mathbf{k}-\mathbf{q}1}$ for an electron-hole (e-h) pair with the electron at $\mathbf{k}+\mathbf{q}$ in the final state $|\Psi^{n2}_{\mathbf{q}2}\rangle$ and the coefficient $Z^{n1}_{\mathbf{k},\mathbf{k}-\mathbf{q}1}$ for an e-h pair with the electron at $\mathbf{k}$ in the initial state $|\Psi^{n1}_{\mathbf{q}1}\rangle$. Figure 1(b) shows that the ex-ph matrix element from the hole scattering process is the hole-phonon matrix element $-M^\nu_{\mathbf{k},\mathbf{k}+\mathbf{q}}(v)$ weighted by the wave function coefficient $Z^{n2*}_{\mathbf{k}+\mathbf{q}2,\mathbf{k}}$ for an e-h pair with the hole at $\mathbf{k}$ in the final state $|\Psi^{n2}_{\mathbf{q}2}\rangle$ and the coefficient $Z^{n1}_{\mathbf{k}+\mathbf{q}2,\mathbf{k}+\mathbf{q}}$ for an e-h pair with the hole at $\mathbf{k}+\mathbf{q}$ in the initial state $|\Psi^{n1}_{\mathbf{q}1}\rangle$.

C. Matrix elements for resonance Raman processes

In the resonance Raman processes as shown in Fig. 2, by absorbing a photon the system is excited from the ground state ($|0\rangle$) to an A_2 excitonic state $|a\rangle$. The exciton then scatters by a phonon from $|a\rangle$ to $|b\rangle$ and is annihilated by emitting a photon.

In either the incident [Fig. 2(a)] or scattered [Fig. 2(b)] resonance processes, there are a real and a virtual excitation state. In the real calculation, the wave function for the virtual state [$|b\rangle$ in Fig. 2(a) and $|a\rangle$ in Fig. 2(b)] is replaced by that of the real state [$|a\rangle$ in Fig. 2(a) and $|b\rangle$ in Fig. 2(b)] as an approximation [see Eq. (12) below]. Thus, the ex-ph matrix element for the resonance Raman processes is that between $|\Psi^n_0(A_2)\rangle$ and $|\Psi^n_0(A_2)\rangle$ states. Then the matrix element of Eq. (8) is simplified as

$$M_{\text{ex-ph}} = \sum_{\mathbf{k}} [M^\nu_{\mathbf{k},\mathbf{k}}(c) - M^\nu_{\mathbf{k},\mathbf{k}}(v)]|Z_{\mathbf{k},\mathbf{k}}|^2. \quad (9)$$

In double-resonance Raman processes (Fig. 3), after absorbing a photon the system is excited from the ground state
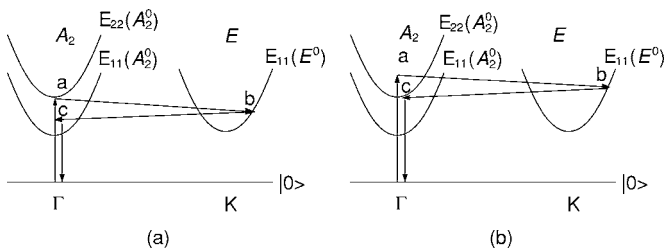
FIG. 3. Double-resonance Stokes Raman processes: (a) incident resonance process and (b) scattered resonance process. The energy difference between the $E_{11}(A^0_2)$ and $E_{11}(E^0)$ states is less than 100 meV and the $E_{11}(A^0_2)$ state lies lower in energy (Ref. 12).
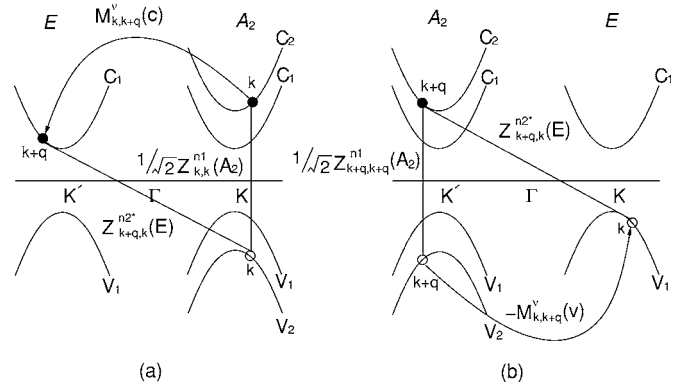
FIG. 4. Electron (a) and hole (b) processes for an ex-ph matrix element between a bright A_2 state and a dark E state. c_1 (c_2) and v_1 (v_2) are used to label the first (second) conduction and valence bands in energies, respectively.

to an A_2 excitonic state $|a\rangle$. The exciton then is scattered by a phonon from state $|a\rangle$ to $|b\rangle$ and is scattered back to $|c\rangle$ by another phonon with an opposite wave vector or by a defect. The exciton is finally annihilated by emitting a photon. For the G' and D Raman bands, the scattering process is intervalley scattering and the $|b\rangle$ state is an E (E^*) exciton. Thus, a G' (D) band process connects an A_2 bright exciton and an E (E^*) dark exciton. The ex-ph matrix element from $|a\rangle$ to $|b\rangle$ in Fig. 3 is then

$$M_{\text{ex-ph}}(a \rightarrow b) = \langle \Psi^{n2}_{\mathbf{q}}(E)|H_{el-ph}|\Psi^{n1}_0(A_2)\rangle. \quad (10)$$

The electron and hole processes for the matrix element $M_{\text{ex-ph}}(a \rightarrow b)$ are shown in Fig. 4, respectively, from which we can get the expression for the matrix element,

$$M_{\text{ex-ph}}(a \rightarrow b) = \frac{1}{\sqrt{2}} \sum_{\mathbf{k}} [M^\nu_{\mathbf{k},\mathbf{k}+\mathbf{q}}(c) Z^{n2*}_{\mathbf{k}+\mathbf{q},\mathbf{k}}(E) Z^{n1}_{\mathbf{k},\mathbf{k}}(A_2)$$
$$- M^\nu_{\mathbf{k},\mathbf{k}+\mathbf{q}}(v) Z^{n2*}_{\mathbf{k}+\mathbf{q},\mathbf{k}}(E) Z^{n1}_{\mathbf{k}+\mathbf{q},\mathbf{k}+\mathbf{q}}(A_2)]. \quad (11)$$

The e-h pairs for the A_2 state in Figs. 4(a) and 4(b) are selected as those around the K and K' points, respectively, and thus a factor $1/\sqrt{2}$ appears in Eq. (11).

Hereafter, we will focus on the first-order resonant Raman process. With the help of Fig. 2, the Stokes Raman intensity per length, I_{ex}, can be written as

$$I_{\text{ex}} = \left| \frac{1}{L} \sum_a \frac{M_{\text{ex-op}}(a) M_{\text{ex-ph}}(a \rightarrow b) M_{\text{ex-op}}(b)}{(E - E_a + i\gamma)(E - E_a - E_{\text{ph}} + i\gamma)} \right|^2$$
$$= \left| \frac{1}{L} \sum_a \frac{M_{\text{ex-op}}(a)^2 M_{\text{ex-ph}}(a \rightarrow a)}{(E - E_a + i\gamma)(E - E_a - E_{\text{ph}} + i\gamma)} \right|^2, \quad (12)$$

where γ is a broadening factor. Here we assume that γ is a constant (0.06 eV).[2,21] In the second expression of Eq. (12), we replace the wave function of the virtual state $|b\rangle$ by that of the real state $|a\rangle$. The reason is that the virtual state $|b\rangle$ is a combination of all the A_2 real states with a zero center-of-mass momentum, and the real state $|a\rangle$ has a dominant component because the energy difference $|E_b - E_a|$ is the smallest
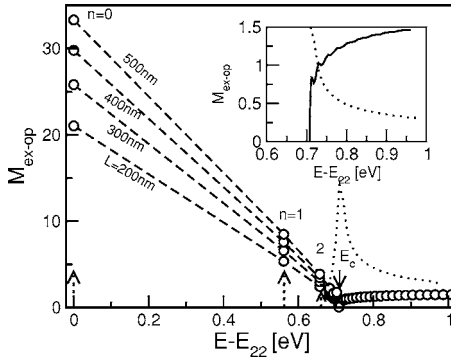
FIG. 5. $M_{\text{ex-op}}$ for $E_{22}(A_{2u}^n)$ states for an (8,0) tube. The continuum band edge E_c is indicated. The dashed lines are a guide to the eyes. The dotted line shows the density of states, and the exciton states are also indicated. The inset is a zoom-in of part of the main figure, but uses different symbols, i.e., solid line instead of white circles.

FIG. 6. $M_{\text{el-op}}$ and $Z_{\mathbf{k}}$ in k space measured from k_{22} for an (8,0) tube. (a) $M_{\text{el-op}}$, (b) the wave function coefficient $Z_{\mathbf{k}}$ for the $E_{22}(A_{2u}^0)$ (dashed line) and for the continuum band edge E_c state (solid line), and (c) $Z_{\mathbf{k}}$ for a continuum band state with an energy $E_c + 0.1$ eV. In (b) $Z_{\mathbf{k}}$ for the $E_{22}(A_{2u}^0)$ state is multiplied by 5.

in this case. Thus, we can set $|b\rangle = |a\rangle$ in Eq. (12). The summation in Eq. (12) is taken for all A_2 states that have a center-of-mass momentum $\mathbf{q} = \mathbf{0}$.

In the free-particle picture, the free *e-h* pair excited by a photon is that with the electron and hole at the same wave vector $\mathbf{k}$. Thus, the Raman intensity per length in the free-particle picture I_{el} is given by

$$I_{\text{el}} = \left| \frac{1}{L} \sum_{\mathbf{k}} \frac{D_{\mathbf{k}}^2 [M_{\text{el-ph}}(\mathbf{k} \rightarrow \mathbf{k}, c) - M_{\text{el-ph}}(\mathbf{k} \rightarrow \mathbf{k}, v)]}{[E - E_{cv}(\mathbf{k}) + i\gamma][E - E_{cv}(\mathbf{k}) - E_{\text{ph}} + i\gamma]} \right|^2.$$

(13)

III. RESULTS AND DISCUSSION

Excitons have both spin singlet and triplet states. The energy difference between them is less than 100 meV,[24] and the spin triplet lies lower in energy. The photon and phonon do not change the spin of the exciton and the triplets are all dark excitons. Thus, in this paper we consider only spin singlet states.

A. Exciton-photon matrix element

For an achiral (armchair or zigzag) SWNT, the exciton wave functions are either even or odd functions of z because of the inversion center in the SWNT. Thus, we use A_u or A_g to label an A exciton in an achiral SWNT, which is symmetric or antisymmetric under a σ_h reflection ($z \rightarrow -z$), respectively.[35] For all A_{2g}^n states, from Eq. (6), we get $M_{\text{ex-op}} = 0$. By using Eq. (6), we calculate $M_{\text{ex-op}}$ for the RBM for an (8,0) SWNT $E_{ii}(A_{2u}^n)$ states for different SWNT lengths $L = 200$, 300, 400, and 500 nm and the results are shown in Fig. 5. It is seen that the matrix element for an excitonic state depends on tube length L, while that for a continuum band state is independent of L. The reason why $M_{\text{ex-op}}$ depends on L is that the number of k points depends on L [see Eq. (6)]. We find that, for an excitonic state, the relationship between $M_{\text{ex-op}}$ and L is $M_{\text{ex-op}} \propto \sqrt{L}$. Moreover, the magnitude of $M_{\text{ex-op}}$ for A_{2u}^0 is about 3.8 times greater

than that for A_{2u}^1. Thus, the Raman intensity for A_{2u}^0 is about $(3.8)^4 \approx 208$ times greater than that for A_{2u}^1. This result can explain why we usually can only probe the Raman signal from the first excitonic state. For a continuum band, $M = 0$ at the band edge $E_c = E_{22} + 0.69$ eV with 0.69 eV the binding energy for the A_{2u}^0 state, and M increases with energy and approaches the matrix element for a free *e-h* pair at the Van Hove singularity (VHS) k_{22}. The wave function for an excitonic state is delocalized in 1D k space. With increasing energy, the delocalized length in k space, i.e., the full width at half maximum amplitude of the wave function coefficient $Z_{\mathbf{k}}$, $\ell_{\mathbf{k}}$, decreases. Hereafter, we neglect the superscript in $Z_{\mathbf{k}}$ for simplicity. When the energy approaches E_c, the wave function in k space is very localized around the VHS as is seen in Fig. 6. The solid and dashed lines in Fig. 6(b) are $Z_{\mathbf{k}}$ for the $E = E_c$ and $E_{22}(A_{2u}^0)$ states, respectively. We can see that $Z_{\mathbf{k}}$ for the E_c state is localized around the VHS $k = 0$ while that for the $E_{22}(A_{2u}^0)$ state is delocalized over the k range. $Z_{\mathbf{k}}$ shows three peaks with the highest peak at k_{22} and two negative peaks on both sides of k_{22} [see Fig. 6(b)]. Thus, the contributions to the optical matrix element from these three peaks are canceled by one-another as can be seen from Figs. 6(a) and 6(b), leading to $M = 0$ at E_c. With energy further increasing from E_c, the peaks of $Z_{\mathbf{k}}$ move away from k_{22} on the two sides [Fig. 6(c), solid line], and from Figs. 6(a) and 6(c) we can see that the optical matrix element is not zero any more. Because of the σ_h reflection symmetry in an (8,0) SWNT, *e-h* pairs at k and $-k$ have the same quasiparticle energy and thus two peaks appear in Fig. 6(c).

From the inset of Fig. 5, we can see that, although the density of states (DOS) of the continuum band has a singularity at E_c, the optical matrix element becomes zero at E_c. Thus, with the energy increasing from E_c, the optical absorption increases from zero to a finite value.
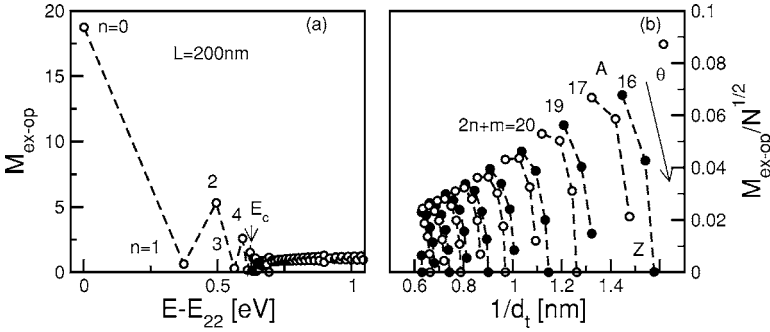
FIG. 7. (a) $M_{\text{ex-op}}$ for $E_{22}(A_2^n)$ states in a (6,5) tube with $L=200$ nm, and (b) the normalized $M_{\text{ex-op}}/N^{1/2}$ for $E_{22}(A_2^1)$ states for all S-SWNTs with $0.6 < d_t < 1.6$ nm. Filled and open circles are for SI and SII SWNTs, respectively. The arrow indicates the θ decreasing direction from armchair (A) to zigzag (Z) SWNTs. In (a), even n states have larger $M_{\text{ex-op}}$ than odd n states and thus in the energy range $E - E_{22} - E_c$ the circles form two lines.

For a zigzag tube, the second A_2 exciton (A_2^1), which is the first A_{2g} exciton (A_{2g}^0), has an exactly zero matrix element $M_{\text{ex-op}}$. For a chiral tube, the σ_h reflection ($z \rightarrow -z$) symmetry does not exist. Thus, it is expected that the A_2^1 state should have a finite $M_{\text{ex-op}}$. Figure 7(a) shows $M_{\text{ex-op}}$ for $E_{22}(A_2^n)$ states for a (6,5) tube with $L=200$ nm. Here it is seen that the A_2^1 state has a nonzero $M_{\text{ex-op}}$ in this case. However, compared to the A_2^0 state, the A_2^1 state has a much smaller $M_{\text{ex-op}}$. Actually, $M_{\text{ex-op}}$ for the A_2^0 state is about 30 times larger than that for the A_2^1 state. Thus, it is hard to observe an optical signal from the A_2^1 state. In Fig. 7(b), we show $M_{\text{ex-op}}$ for the $E_{22}(A_2^1)$ state (the second excited exciton) for all tubes with $0.6 < d_t < 1.6$ nm. It is seen that the matrix element strongly depends on the tube diameter and chiral angle. $M_{\text{ex-op}}$ has a maximum value for a tube closest to an armchair tube, while it becomes zero for a zigzag tube. We should mention that although the optical matrix element for the $E_{22}(A_2^1)$ state strongly depends on both the tube diameter and chiral angle, the matrix element for the $E_{22}(A_0^1)$ state only depends on the tube diameter and does not depend on the tube chiral angle as will be shown below (see Fig. 9).

From Figs. 5 and 7, we can see that the A_2^0 state has a much larger $M_{\text{ex-op}}$ than the other excited exciton A_2^n ($n > 1$) states. We can understand this result from the different shapes of the wave function coefficient $Z_{\mathbf{k}}$ of A_2^n states. Explicitly, $Z_{\mathbf{k}}$ of A_2^0 is a Gaussian-like function with no node and that of A_2^1 is an odd function $(k-k_{ii})e^{-\alpha(k-k_{ii})^2}$ with one node around k_{ii}.[24] $M_{\text{el-op}}$ is either symmetric (achiral SWNTS) or nearly symmetric (chiral SWNTs) with respect to k_{ii} (see Fig. 6). Therefore, from Eq. (6), we know that for the A_2^0 state, the contribution to $M_{\text{ex-op}}$ from all $Z_{\mathbf{k}}$ at different k are added to each other, leading to a large M. For the A_2^1 state, the contributions to $M_{\text{ex-op}}$ from $Z_{\mathbf{k}}$ on different sides of the node cancel each other (or they partially cancel), leading to a zero (or small) $M_{\text{ex-op}}$ value. For the A_0^n state with n

$=2,3,\ldots$, the number of nodes is more than 1 and the contributions to $M_{\text{ex-op}}$ from the positive and negative parts of $Z_{\mathbf{k}}$ are either canceled or partially canceled, leading to a zero or small $M_{\text{ex-op}}$ value. The large $M_{\text{ex-op}}$ in A_2^0 is mainly due to the special shape of its $Z_{\mathbf{k}}$, which has no node. With increasing n, the $Z_{\mathbf{k}}$ delocalized length decreases, which also contributes to a decrease of the optical matrix element.

The exciton binding energy (E_{bd}) for a M-SWNT is generally one order of magnitude smaller than that of a S-SWNT with a similar d_t.[11,24] As a result, the peak of $Z_{\mathbf{k}}$ for the M-SWNT is sharper than that for the S-SWNT. However, the peak of the M-SWNT is not sharp enough around k_{ii} and thus $M_{\text{ex-op}}$ for the M-SWNT is only a bit smaller than that for the S-SWNT. For example, the chiral tubes (6,5) and (7,4) have diameters $d_t=0.73$ and 0.74 nm, respectively. The binding energy for (6,5) and (7,4) tubes is $E_{\text{bd}}=0.63$ and 0.07 eV, respectively, which can be seen from Figs. 7(a) and 8(a). Furthermore, the half width ℓ_k in Fig. 8(b) for (6,5) and (7,4) SWNTs is about $0.38/a$ and $0.21/a$, respectively, with a denoting the length of graphite unit cell vector. The peak of $Z_{\mathbf{k}}$ in Fig. 8(b) for the (7,4) SWNT is not sharp enough around k_{11L} and thus with $L=200$ nm, $M_{\text{ex-op}}/M_{\text{el-op}}=10.5$ for the (7,4) SWNT, which is a bit smaller than $M_{\text{ex-op}}/M_{\text{el-op}}=15.4$ for the (6,5) SWNT.

To see the tube type and chirality dependences of $M_{\text{ex-op}}$, we calculate the normalized (per two carbon atoms) $M_{\text{ex-op}}/N^{1/2}$ for $E_{11}(A_2^0)$ and $E_{22}(A_2^0)$ states for S-SWNTs and $E_{11L}(A_2^0)$ states for M-SWNTs and the results are shown in Fig. 9(a). Here N is the number of graphite unit cells in a SWNT. We find that $M_{\text{ex-op}}$ for $E_{ii}(A_2^0)$ states shows a $1/d_t$ dependence, while $M_{\text{ex-op}}$ shows no tube type or chiral angle dependence. Thus, the optical absorption intensity in SWNTs is expected to show $(1/d_t)^2$ dependence but no tube type nor chirality dependences. Moreover, $E_{22}(A_2^0)$ states have a larger $M_{\text{ex-op}}$ than $E_{11}(A_2^0)$ states because $E_{22}(A_2^0)$ states have a larger binding energy and thus a more localized exciton wave
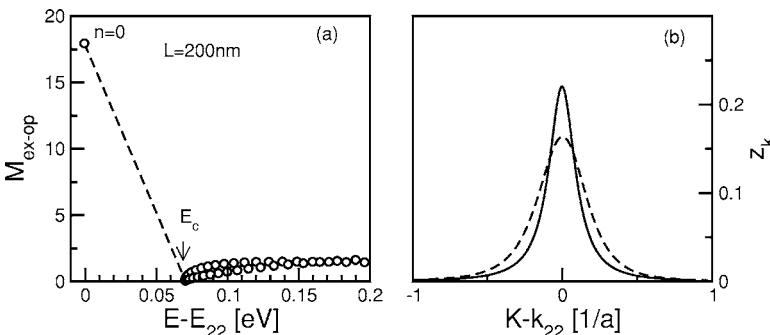
FIG. 8. $M_{\text{ex-op}}$ and $Z_{\mathbf{k}}$ for various states in a (7,4) M-SWNT. (a) $M_{\text{ex-op}}$ for $E_{11L}(A_2^n)$ with $L=200$ nm and (b) Z_k for $E_{11L}(A_2^0)$ (solid line). Z_k for $E_{22}(A_2^0)$ for a (6,5) SWNT is also shown (dashed line). All $E_{11L}(A_2^n)$ ($n > 2$) states belong to continuum band states.
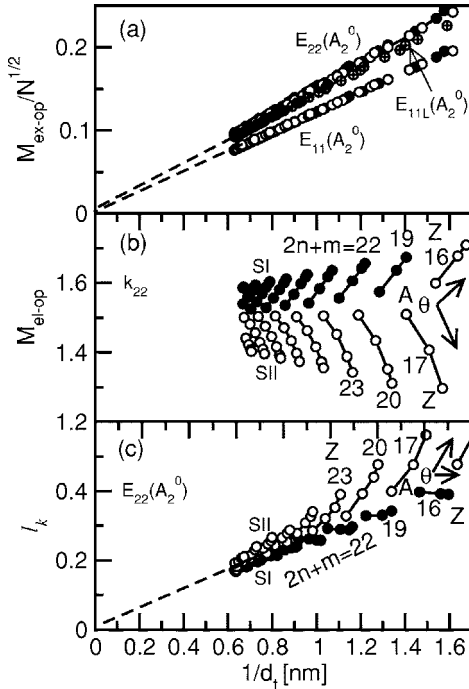
FIG. 9. Tube diameter dependence of $M_{\text{ex-op}}/N^{1/2}$, $M_{\text{el-op}}$, and $\ell_{\mathbf{k}}$ in SWNTs with $0.6 < d_t < 1.6$ nm. Filled, open, and crossed circles are for SI-, SII-, and M-SWNTs, and (a) $M_{\text{ex-op}}$ for $E_{22}(A_2^0)$, $E_{11}(A_2^0)$ of S-SWNTs and $E_{11L}(A_2^0)$ of M-SWNTs, (b) $M_{\text{el-op}}$ at k_{22}, and (c) $\ell_{\mathbf{k}}$ for $E_{22}(A_2^0)$. The arrows in (b) and (c) indicate the directions along which θ is decreasing (A, armchair side; Z, zigzag side).

function.[24] Interestingly, $E_{11L}(A_2^0)$ states of M-SWNTS have a slightly smaller $M_{\text{ex-op}}$ than $E_{22}(A_2^0)$ states of S-SWNTs. The reason is that the wave function for $E_{11L}(A_2^0)$ states of M-SWNTs is more delocalized than that for $E_{22}(A_2^0)$ states of S-SWNTs and $M_{\text{el-op}}$ at k_{11L} of M-SWNTs has a larger magnitude than that at k_{22} of S-SWNTs.

In the free-particle picture, $M_{\text{el-op}}$ shows almost no d_t dependence, while it has some tube type and chiral angle dependences as shown in Fig. 9(b). As a result, the tube type and chirality dependences of the optical absorption intensity in the exciton and free-particle pictures are completely different and our predicted dependences in the exciton picture are expected to be confirmed by future experiments. We can understand the disappearance of tube type and chirality dependences of $M_{\text{ex-op}}$ as follows. The localization of the exciton wave function increases the optical matrix element from that for a free e-h pair. This enhancement effect can be characterized by $\ell_{\mathbf{k}}$, the half-width of $Z_{\mathbf{k}}$ in k space. An excitonic state with a larger ℓ_k has a larger $M_{\text{ex-op}}$. Figure 9(c) shows ℓ_k for $E_{22}(A_2^0)$ states of S-SWNTs. Figure 9(b) plots the el-op matrix element $M_{\text{el-op}}$ at k_{22} of S-SWNTs. Figure 9(b) indicates that SI tubes have a larger $M_{\text{el-op}}$ than SII tubes, while Fig. 9(c) shows that SI tubes have a smaller ℓ_k than SII tubes, leading to no tube type dependence of $M_{\text{ex-op}}$ for $E_{22}(A_2^0)$ states in Fig. 9(a). Similarly, both SI and SII tubes have an opposite family spreading tendency for $M_{\text{el-op}}$ and ℓ_k in Figs. 9(b) and 9(c), leading to no chiral dependence of $M_{\text{ex-op}}$ for $E_{22}(A_2^0)$ states in Fig. 9(a). The $1/d_t$ dependence of $M_{\text{el-op}}$ for $E_{22}(A_2^0)$ states in Fig. 9(a) is from the $1/d_t$ depen-
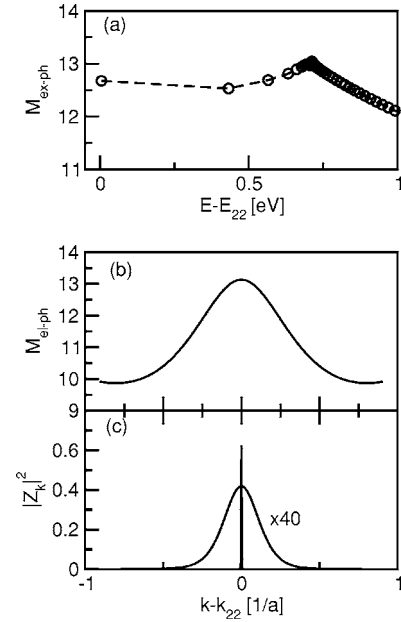
FIG. 10. RBM $M_{\text{ex-ph}}$ for $E_{22}(A_2^n)$, $M_{\text{el-ph}}$ at k_{22}, and $|Z_{\mathbf{k}}|^2$ for the $E_{22}(A_2^0)$ and $E = E_c$ states for an (8,0) tube. (a) $M_{\text{ex-ph}}$ as a functions of $E - E_{22}$. (b) $M_{\text{el-op}}$, and (c) $Z_{\mathbf{k}}$ as functions and of $k - k_{22}$ in units of $1/a$. $|Z_{\mathbf{k}}|^2$ for the E_c state is a δ-like function at k_{22}. $|Z_{\mathbf{k}}|^2$ for $E_{22}(A_2^n)$ has been multiplied by 40. For both the $E_{22}(A_2^0)$ and E_c states, $|Z_{\mathbf{k}}|^2$ is normalized to the units taken for the integration of k.

dence of ℓ in Fig. 9(c). For the same reasons, $M_{\text{ex-op}}$ for $E_{11}(A_2^0)$ states of S-SWNTs and $E_{11L}(A_2^0)$ states of M-SWNTs also show a $1/d_t$ dependence but no tube type or chiral angle dependences.

B. Exciton-phonon matrix element

The ex-ph matrix elements $M_{\text{ex-ph}}$ for the RBM and G-band modes are calculated by using Eq. (9). Figure 10(a) shows the RBM $M_{\text{ex-ph}}$ for $E_{22}(A_2^n)$ states for an (8,0) SWNT. Unlike $M_{\text{ex-op}}$, $M_{\text{ex-ph}}$ is not sensitive to the excitation energy. All excitonic states have a similar $M_{\text{ex-ph}}$. Moreover, the E_c state has a maximum $M_{\text{ex-ph}}$, which is equal to $M_{\text{el-ph}}$ for a free e-h pair at k_{22}. From Fig. 10(b), we can see that $M_{\text{el-ph}}$ in the free-particle picture has a maximum at k_{22} and it decreases slowly in the $|Z_{\mathbf{k}}|^2$ delocalized region. Moreover, Fig. 10(c) shows that $|Z_{\mathbf{k}}|^2$ for the E_c state is a δ-like function at k_{22}. Therefore, from the A_2^0 exciton state to the continuum band edge E_c state, $M_{\text{ex-ph}}$ varies from 12.8 to a maximum of 13.2.

The RBM matrix element $M_{\text{ex-ph}}$ for $E_{22}(A_2^0)$ for all S-SWNTs with $0.6 < d_t < 1.6$ nm is shown in Fig. 11. For comparison, the corresponding matrix elements for free electrons and holes at k_{22} are also shown. As expected, Fig. 11 shows that $M_{\text{ex-ph}}$ and $M_{\text{el-ph}}$ are almost the same.

We also calculated $M_{\text{ex-ph}}$ for the G-band modes. As shown in Figs. 12(a) and 12(b), for the LO mode $M_{\text{ex-ph}}$ and $M_{\text{el-ph}}$ are similar. For the TO mode, the exciton-phonon matrix element is zero for a zigzag SWNT and it increases with chiral angle. For the TO mode, the excitonic effect decreases the phonon matrix element value for a SWNT with a large chiral angle [see Figs. 12(c) and 12(d)].
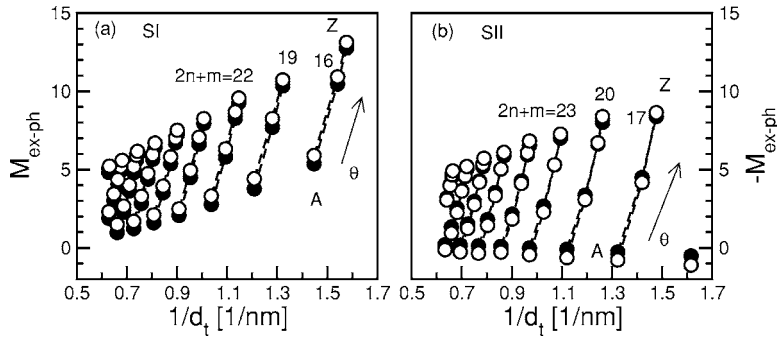
FIG. 11. RBM matrix elements $M_{\text{ex-ph}}$ (filled) for $E_{22}(A_2^0)$ and $M_{\text{el-ph}}$ (open) around k_{22} for all S-SWNTs with $0.6 < d_t < 1.6$ nm for (a) SI and (b) SII tubes. The arrows indicate the direction along which θ is decreasing (A, armchair side; Z, zigzag side).

Figure 13 gives $M_{\text{el-ph}}$ for the LO and TO modes in k space for a (6,5) tube. From Figs. 10 and 13, we can see that around k_{22}, the curve for $M_{\text{el-ph}}$ has a similar shape for the LO and RBM modes. Moreover, in the $|Z_{\mathbf{k}}|^2$ delocalized region, $M_{\text{el-ph}}$ varies more quickly for the LO mode than for the RBM, leading to a larger relative difference between $M_{\text{ex-ph}}$ and $M_{\text{el-ph}}$ in the LO mode (see Figs. 11 and 12). The curve for the TO mode is asymmetric around $k=k_{22}$. For the TO mode, $|M_{\text{el-ph}}|$ on the left and right sides of k_{22} is, respectively, smaller and larger than $|M_{\text{el-ph}}|$ at k_{22}, and around k_{22} the curve on the left side changes more quickly than that on the right side. As a result, $M_{\text{ex-ph}}$ is smaller than $M_{\text{el-ph}}$ at k_{22}.

From Figs. 11 and 12, we can see that for the RBM and G-band modes, $M_{\text{ex-ph}}$ for $E_{22}(A_2^0)$ and $M_{\text{el-ph}}$ at k_{22} are generally similar. In particular, the relative difference between $M_{\text{ex-ph}}$ and $M_{\text{el-ph}}$ is very small for the RBM and it is also within 5% for the LO mode. For the TO mode, the excitonic effect decreases the matrix element for SWNTs with a large chiral angle. We should mention that the above conclusion is valid for all E_{ii} cases.

There are also differences between the el-ph matrix elements by the STB and ETB models for the RBM, especially

for smaller-d_t tubes.[31] In the STB model, the σ orbital is not included and thus the curvature effect is not well incorporated into the STB model. We partially include the curvature effect by putting the π orbital perpendicular to the tube sidewall. In this way, the contribution to the matrix element from the next-nearest neighbors is overestimated. As a result, $M_{\text{el-ph}}$ has a larger value for the RBM than for the LO mode. By including a σ orbital contribution, the magnitude of $M_{\text{el-ph}}$ for the RBM decreases and it has a smaller value than that for the LO mode. Although the absolute values of the $M_{\text{el-ph}}$ for the RBM calculated by the STB and ETB models are different from each other, the tube type and chirality dependences of $M_{\text{el-ph}}$ as calculated by the STB and ETB models give similar results. As we have mentioned, the similarity between $M_{\text{ex-ph}}$ and $M_{\text{el-ph}}$ comes from the fact that the relative changes of $M_{\text{el-ph}}$ around k_{ii} are small. By considering that the relative changes of $M_{\text{el-ph}}$ around k_{ii} by the ETB and STB models are almost the same, the above conclusions for the STB should not change when considering the ETB model.

Equation (8) indicates that the ex-ph matrix element is a product of the exciton wave function coefficients for the initial and final states and the el-ph matrix element between the initial and final states. The same formula was used in the study of the sidebands in the optical absorption spectra due to a strong ex-ph coupling in SWNTs.[18] Also, we expect that the exciton wave function coefficients obtained here and those from Ref. 18 should be similar to each other because the coefficients in both cases are obtained by solving the BS equation within the STB model and the wave functions are not sensitive to the treatment of the electron screening ef-
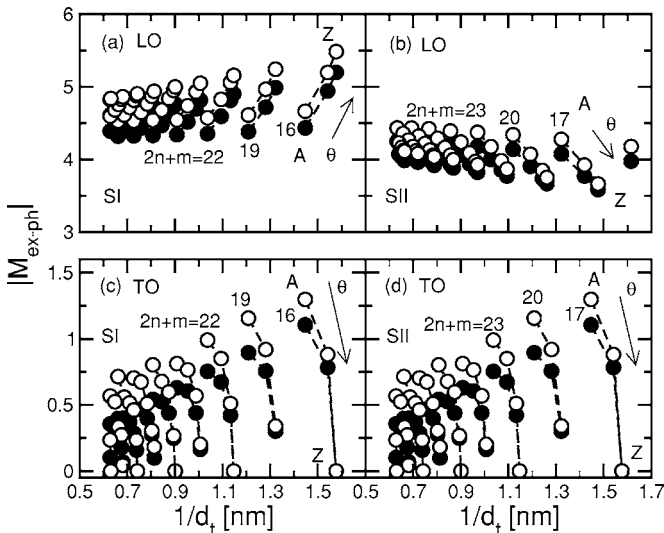
FIG. 12. LO and TO mode matrix elements $M_{\text{ex-ph}}$ for $E_{22}(A_2^0)$ (filled) and $M_{\text{el-ph}}$ at k_{22} (open) for all S-SWNTs with $0.6 < d_t < 1.6$ nm. LO mode for (a) SI tubes and (b) SII tubes. TO mode for (c) SI tubes and (d) SII tubes. In (c) and (d), $M_{\text{ex-ph}} = M_{\text{el-ph}} = 0$ for zigzag tubes. The arrows indicate the direction along which θ is decreasing (A, armchair side; Z, zigzag side).
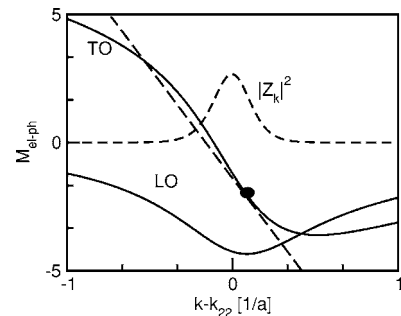
FIG. 13. $M_{\text{el-ph}}$ (solid lines) for LO and TO modes in 1D k space for a (6,5) tube. $|Z_{\mathbf{k}}|^2$ (dashed line) for the $E_{22}(A_2^0)$ state, and a line tangential to the curve for the TO mode at the right side of k_{22} (dot) are also shown (long-dashed line).
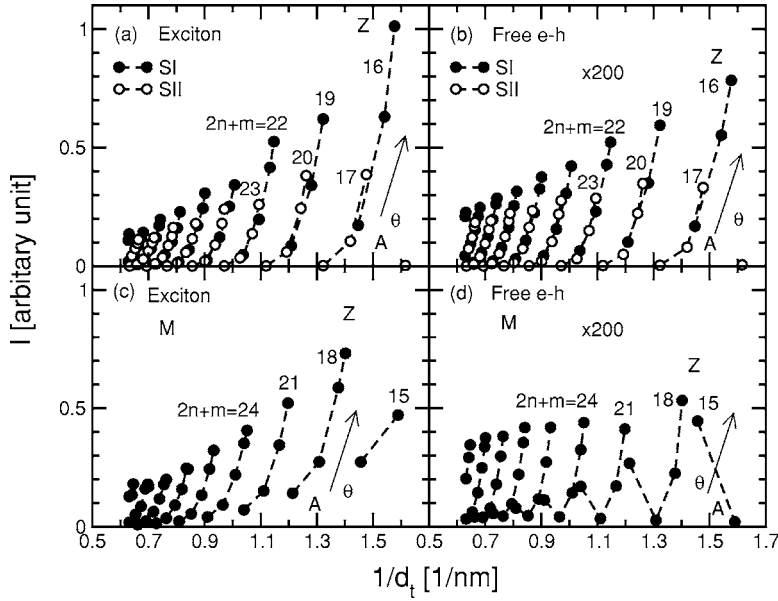
FIG. 14. RBM Raman intensity per length for SWNTs with $0.6 < d_t < 1.6$ nm. (a) and (b) are for $E_{22}(A_2^0)$ and free *e-h* at k_{22} in S-SWNTs, respectively. Filled and open circles are for SI and SII tubes. (c) and (d) are for $E_{11L}(A_2^0)$ and free *e-h* at k_{11L} in M-SWNTs, respectively. The intensity in the free el-ph case has been multiplied by 200. The arrows indicate the θ decreasing direction (A, armchair side; Z, zigzag side). In (d), within a family the armchair tube has a larger intensity than its neighbor due to a node effect.

fects. Moreover, we calculate the el-ph matrix elements from the deformation potential.[21,28–33] For the LO and A_1 modes, which show strong sideband peaks as found in Ref. [18], the treatments of the el-ph matrix element by using the deformation potential as in the present work or the Su-Schrieffer-Heeger (SSH) model as used in Ref. [18] are approximately equivalent to each other.[31] For the RBM, the curvature effect is important in the el-ph coupling. However, we found that the effect of curvature on the el-ph coupling through the σ orbital is partially canceled by the contributions from (p_z, p_z) and those from (p_x, p_z), (p_z, p_x) and (p_y, p_z), (p_z, p_y),[31] and thus the SSH model can approximately describe the el-ph coupling for the RBM. Therefore, the ex-ph couplings for the RBM, LO, and A_1 modes as calculated by our method should be similar to those calculated by Perebeinos *et al.*,[18] though the detailed behaviors of each quantity might be different to some extent. We should mention that the on-site deformation potential, which is not included in the work of Perebeinos *et*

al.,[18] brings in nonzero ex-ph matrix elements for two E_1' modes, which is important in explaining the experimentally observed Raman mode around 2450 cm^{-1} in carbon.[31] As we have seen from the present calculations, the ex-ph matrix elements for the RBM and LO modes do show chirality dependences and thus some chirality dependences are also expected to be shown in the optical absorption intensities for the RBM and LO sidebands because the sideband intensity is proportional to the absolute square of the ex-ph matrix element.[18]

C. Resonance Raman intensity for the RBM and *G* band

We calculate the resonant Raman intensity for the RBM by using Eq. (12). For an S-SWNT, the energy spacing between the $E_{ii}(A_2^0)$ and $E_{ii}(A_2^1)$ states is sufficiently large compared with the resonance window γ and thus we only need to consider one exciton state A_2^0 in Eq. (12) in the calculation of
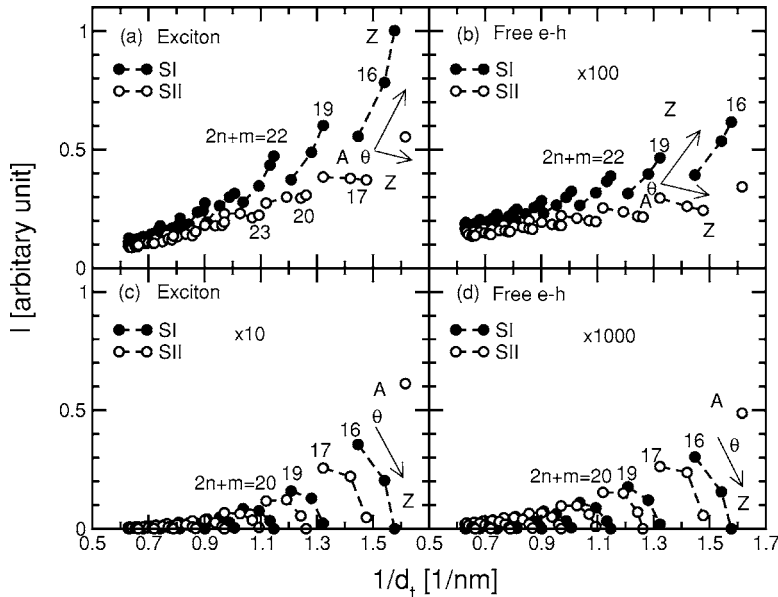
FIG. 15. *G*-band Raman intensities per length in S-SWNTs with $0.6 < d_t < 1.6$ nm. (a) and (b) are for the LO mode with (a) for $E_{22}(A_2^0)$ excitonic states and (b) for free *e-h* k_{22} states. Filled and open circles are for SI and SII tubes. (c) and (d) are for the TO mode with (c) for $E_{22}(A_2^0)$ excitonic states and (d) for free *e-h* states at k_{22}. The intensity in the free *e-h* case has been multiplied by 100 (b) and 1000 (d). The arrows indicate the θ decreasing direction (A, armchair side; Z, zigzag side).
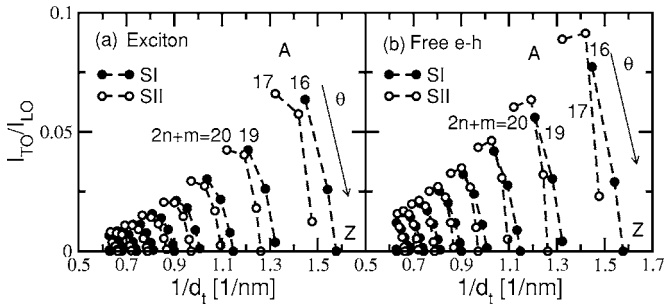
FIG. 16. The Raman intensity ratio between the TO and LO modes, I_{TO}/I_{LO}, in S-SWNTs with $0.6 < d_t < 1.6$ nm. (a) and (b) are for the exciton and free e-h pictures, respectively. The arrows indicate the θ decreasing direction (A, armchair side; Z, zigzag side).

the Raman intensity resonant with the $E_{ii}(A_2^0)$ energy. For an M-SWNT, the energy spacing between the $E_{iiL}(A_2^0)$ and $E_{iiL}(A_2^1)$ states is comparable to or smaller than the resonance width γ.[36] Moreover, the energy spacing between $E_{iiL}(A_2^0)$ and $E_{iiH}(A_2^0)$ is also comparable to or smaller than γ for tubes with a large chiral angle and thus a quantum interference effect occurs.[21,37] Therefore, in the calculations of the intensity resonant with the $E_{iiL}(A_2^0)$ energy for M-SWNTs, we take a summation over many $E_{iiL}(A_2^0)$ and $E_{iiH}(A_2^0)$ exciton states in Eq. (12). The intensities per length for the $E_{22}(A_2^0)$ and $E_{11L}(A_2^0)$ in S-SWNTs and M-SWNTs are shown in Figs. 14(a) and 14(c), respectively. The intensities for free e-h by Eq. (13) are also shown in Figs. 14(b) and 14(d). We can see that the exciton and free-particle pictures yield the same tube type and similar chiral angle dependences, and as expected the excitonic effect enhances the diameter dependence. Moreover, the excitonic effect enhances the magnitude of the intensity by enhancing the optical matrix element. Equation (12) indicates that $I \propto (M_{ex\text{-}op})^4$. For a SWNT with $L = 200$ nm, $M_{ex\text{-}op}/M_{el\text{-}op}$ is about 10 and I_{ex}/I_{el} is about 10^4 if we do not take the summation over k in Eq. (13) into account. I_{el} is enhanced by the DOS at E_{ii} and thus I_{ex}/I_{el} is about 10^2 in Fig. 14. Interestingly, Fig. 14 shows the same order of magnitude for the RBM Raman intensity for M-SWNTs and S-SWNTs, which is consistent with experiments. The reason is that the optical matrix elements for a M-SWNT and S-SWNT with a similar d_t have a similar value.

The Raman intensity for the G-band modes is also calculated. The results are shown in Fig. 15. Similar to the RBM case, the shapes of the curves in Figs. 15(a) and 15(c) for the excitonic model are similar to those of Figs. 15(b) and 15(d) for the free-particle model, respectively. The excitonic effect also enhances the diameter dependence and magnitude of the intensity. From Figs. 14(a), 15(a), and 15(c), it is seen that the LO mode has a weaker chiral angle dependence compared to the RBM and TO modes. Moreover, Fig. 15(a) shows a family pattern similar to that in the excitation energy Kataura plot.[3]

Motivated by the observations that the excitonic effect almost does not change the phonon matrix element for the LO mode, while it decreases the phonon matrix element for the TO mode, we find that the excitonic effect decreases the Raman intensity ratio between the TO and LO modes. We calculate the Raman intensity ratio I_{TO}/I_{LO} and the results are shown in Fig. 16. We can see that I_{TO}/I_{LO} in the exciton picture is generally smaller than that in the free e-h picture. Moreover, I_{TO}/I_{LO} is largest for the SWNTs with a chiral angle closest to the armchair tubes and it becomes zero for zigzag SWNTs. The intensity ratio in Fig. 16 also shows clear family patterns. In view of the experiments, the environmental dielectric constants can be varied from close to 1 to a large value by putting the SWNT samples in air or water. Thus the excitonic effect varies in the different SWNT samples and the Raman intensity ratio I_{TO}/I_{LO} is expected to be smaller for the SWNT samples with a smaller environmental dielectric constant.

From Figs. 14 and 15, we can draw the conclusion that for calculating the resonant Raman intensity, the exciton and free-particle models generally yield the same tube type and a similar chirality dependence. The excitonic effect increases the diameter dependence and the absolute value of the intensity. Within the excitonic picture, the diameter dependence for the RBM intensity within the diameter range observed experimentally in Ref. 23 is about four times stronger than within the free electron-hole picture. Therefore, our calculations now predict the observed intensity diameter-dependent trend shown in Ref. 23. This shows another important result where excitons have to be considered, and that excitonic calculations now have to be carried out to obtain photoluminescence intensities.[32]

In summary, we have calculated the ex-op and ex-ph matrix elements and the Raman intensities for the RBM and G-band phonon modes. The relations between the ex-op and el-op matrix elements and those between the ex-ph and el-ph matrix elements are understood from the exciton wave function, and from the el-op and el-ph matrix elements as a function of k around a VHS. We found that, unlike the free-particle picture, the optical absorption intensity in the exciton picture shows a $(1/d_t)^2$ dependence but no tube type or chiral angle dependences. Moreover, we demonstrate that, although the free-particle picture can generally describe the RBM and G-band Raman intensities, the localization of the exciton wave function greatly enhances the Raman signal and the intensity of the d_t dependence. Moreover, the Raman intensity in metallic tubes shows excitonic-like behavior rather than free-particle-like behavior.

[1] R. Saito, G. Dresselhaus, and M. S. Dresselhaus, *Physical Properties of Carbon Nanotubes* (Imperial College Press, London, 1998).

[2] A. Jorio, C. Fantini, M. A. Pimenta, R. B. Capaz, Ge. G. Samsonidze, G. Dresselhaus, M. S. Dresselhaus, J. Jiang, N. Kobayashi, A. Grüneis, and R. Saito, Phys. Rev. B **71**, 075401 (2005).

[3] Ge. G. Samsonidze, R. Saito, N. Kobayashi, A. Grüneis, J. Jiang, A. Jorio, S. G. Chou, G. Dresselhaus, and M. S. Dresselhaus, Appl. Phys. Lett. **85**, 5703 (2004).

[4] R. Saito, K. Sato, Y. Oyama, J. Jiang, Ge. G. Samsonidze, G. Dresselhaus, and M. S. Dresselhaus, Phys. Rev. B **72**, 153413 (2005).

[5] M. J. O'Connell, S. M. Bachilo, X. B. Huffman, V. C. Moore, M. S. Strano, E. H. Haroz, K. L. Rialon, P. J. Boul, W. H. Noon, C. Kittrell, J. Ma, R. H. Hauge, R. B. Weisman, and R. E. Smalley, Science **297**, 593 (2002).

[6] S. M. Bachilo, M. S. Strano, C. Kittrell, R. H. Hauge, R. E. Smalley, and R. B. Weisman, Science **298**, 2361 (2002).

[7] A. Jorio, A. G. Souza Filho, G. Dresselhaus, M. S. Dresselhaus, R. Saito, J. H. Hafner, C. M. Lieber, F. M. Matinaga, M. S. S. Dantas, and M. A. Pimenta, Phys. Rev. B **63**, 245416 (2001).

[8] M. S. Dresselhaus, Ge. G. Samsonidze, S. G. Chou, G. Dresselhaus, J. Jiang, R. Saito, and A. Jorio, Physica E (Amsterdam) **29**, 443 (2005).

[9] M. S. Dresselhaus, G. Dresselhaus, R. Saito, and A. Jorio, Phys. Rep. **409**, 47 (2005).

[10] C. Fantini, A. Jorio, M. Souza, M. S. Strano, M. S. Dresselhaus, and M. A. Pimenta, Phys. Rev. Lett. **93**, 147406 (2004).

[11] C. D. Spataru, Sohrab Ismail-Beigi, Lorin X. Benedict, and Steven G. Louie, Phys. Rev. Lett. **92**, 077402 (2004).

[12] C. D. Spataru, S. Ismail-Beigi, R. B. Capaz, and S. G. Louie, Phys. Rev. Lett. **95**, 247402 (2005).

[13] F. Wang, G. Dukovic, L. E. Brus, and T. F. Heinz, Science **308**, 838 (2005).

[14] J. Maultzsch, R. Pomraenke, S. Reich, E. Chang, D. Prezzi, A. Ruini, E. Molinari, M. S. Strano, C. Thomsen, and C. Lienau, Phys. Rev. B **72**, 241402(R) (2005).

[15] T. Ando, J. Phys. Soc. Jpn. **66**, 1066 (1997).

[16] E. Chang, G. Bussi, A. Ruini, and E. Molinari, Phys. Rev. Lett. **92**, 196401 (2004).

[17] V. Perebeinos, J. Tersoff, and Ph. Avouris, Phys. Rev. Lett. **92**, 257402 (2004).

[18] V. Perebeinos, J. Tersoff, and Ph. Avouris, Phys. Rev. Lett. **94**, 027402 (2005).

[19] F. Plentz, H. B. Ribeiro, A. Jorio, M. S. Strano, and M. A. Pimenta, Phys. Rev. Lett. **95**, 247401 (2005).

[20] S. K. Doorn, D. A. Heller, P. W. Barone, M. L. Usrey, and M. S. Strano, Appl. Phys. A: Mater. Sci. Process. **78**, 1147 (2004).

[21] J. Jiang, R. Saito, A. Grüneis, S. G. Chou, Ge. G. Samsonidze, A. Jorio, G. Dresselhaus, and M. S. Dresselhaus, Phys. Rev. B **71**, 205420 (2005).

[22] M. Machón, S. Reich, H. Telg, J. Maultzsch, P. Ordejón, and C. Thomsen, Phys. Rev. B **71**, 035416 (2005).

[23] A. Jorio, C. Fantini, M. A. Pimenta, D. A. Heller, M. S. Strano, M. S. Dresselhaus, Y. Oyama, J. Jiang, and R. Saito, Appl. Phys. Lett. **88**, 023109 (2006).

[24] J. Jiang, R. Saito, Ge. G. Samsonidze, A. Jorio, S. G. Chou, G. Dresselhaus, and M. S. Dresselhaus, Phys. Rev. B (to be published).

[25] G. Dukovic, F. Wang, D. Song, M. Y. Sfeir, T. F. Heinz, and L. E. Brus, Nano Lett. **5**, 2314 (2005).

[26] J. Jiang, R. Saito, A. Grüneis, G. Dresselhasu, and M. S. Dresselhasu, Carbon **42**, 3169 (2004).

[27] A. Grüneis, R. Saito, Ge. G. Samsonidze, T. Kimura, M. A. Pimenta, A. Jorio, A. G. Souza Filho, G. Dresselhaus, and M. S. Dresselhaus, Phys. Rev. B **67**, 165402 (2003).

[28] J. Jiang, R. Saito, A. Grüneis, G. Dresselhaus, and M. S. Dresselhaus, Chem. Phys. Lett. **392**, 383 (2004).

[29] J. Jiang, R. Saito, A. Grüneis, S. G. Chou, Ge. G. Samsonidze, A. Jorio, G. Dresselhaus, and M. S. Dresselhaus, Phys. Rev. B **71**, 045417 (2005).

[30] A. Grüneis, Ph.D. thesis, Department of Physics, Tohoku University, Sendai, Japan, 2004.

[31] J. Jiang, R. Saito, Ge. G. Samsonidze, S. G. Chou, A. Jorio, G. Dresselhaus, and M. S. Dresselhaus, Phys. Rev. B **72**, 235408 (2005).

[32] Y. Oyama, R. Saito, K. Sato, J. Jiang, Ge. G. Samsonidze, A. Gruneis, Y. Miyauchi, S. Maruyama, A. Jorio, G. Dresselhaus, and M. S. Dresselhaus, Carbon **44**, 873 (2006).

[33] K. Sato, R. Saito, Y. Oyama, J. Jiang, L. G. Cançado, M. A. Pimenta, A. Jorio, Ge. G. Samsonidze, G. Dresselhaus, and M. S. Dresselhaus, Chem. Phys. Lett. **427**, 117 (2006).

[34] R. Saito, A. Grüneis, Ge. G. Samsonidze, G. Dresselhaus, M. S. Dresselhaus, A. Jorio, L. G. Cançado, M. A. Pimenta, and A. G. Souza, Appl. Phys. A: Mater. Sci. Process. **78**, 1099 (2004).

[35] E. B. Barros, R. B. Capaz, A. Jorio, Ge. G. Samsonidze, A. G. Souza Filho, S. Ismail-Beigi, C. D. Spataru, S. G. Louie, G. Dresselhaus, and M. S. Dresselhaus, Phys. Rev. B **73**, 241406(R) (2006).

[36] J. S. Park, Y. Oyama, R. Saito, W. Izumida, J. Jiang, K. Sato, C. Fantini, A. Jorio, G. Dresselhaus, and M. S. Dresselhaus, Phys. Rev. B **74**, 165414 (2006).

[37] S. G. Chou, F. P. Filho, J. Jiang, R. Saito, D. Nezich, H. B. Ribeiro, A. Jorio, M. A. Pimenta, Ge. G. Samsonidze, A. P. Santos, M. Zheng, G. B. Onoa, E. D. Semke, G. Dresselhaus, and M. S. Dresselhaus, Phys. Rev. Lett. **94**, 127402 (2005).